In-line XPS for advanced semiconductor manufacturing and metrology on fully integrated targets

Christopher J. Lee*[a], Manasa Medikonda[a], Trevor McDonough[a], Will Parkin[a], Ruqiang Bao[a], Paul Isbester[b], Mark Klare[b], and Daniel Schmidt[a]
[a]IBM Research, 257 Fuller Road, Albany, NY 12203, USA
[b]Nova Measuring Instruments Inc., 3342 Gateway Blvd, Fremont, CA 94538, USA

ABSTRACT

The continual demands to shrink device sizes and length scales in the semiconductor industry have accelerated the adoption of X-ray photoelectron spectroscopy (XPS) as a critical step for in-line metrology. The technique was initially introduced to the in-line environment to measure ultrathin layers and layer stacks predominantly in the gate module. As these stacks and related structures increase in complexity through scaling, a more rigorous assignment of spectral components to their material intensity source is necessary to use the full potential of XPS. In this paper, the application areas for in-line XPS are reviewed and modeling practices are demonstrated that significantly enhance XPS measurement characterization related to gate-all-around (GAA) transistor architectures. Besides traditional measurements on non-patterned areas, the high surface sensitive nature of XPS may also be tailored specifically for use on fully integrated targets. For example, successful quantification of material residues remaining on active device areas is presented and discussed. Such measurements directly on device are particularly significant as dedicated measurement targets may not serve as a proxy for active areas anymore. The need for advanced XPS modeling capabilities beyond 1D film stack characterization and towards direct 2D/3D measurement on fully integrated structures will be highlighted.

Keywords: X-ray photoelectron spectroscopy, gate-all-around, in-line metrology, in-line XPS, advanced XPS, XRF

*Corresponding author: chris.j.lee@ibm.com

1. INTRODUCTION

Over the past couple decades, X-ray photoelectron spectroscopy (XPS) has emerged as a critical metrology technique in the semiconductor manufacturing environment as scaling demands of the industry drive characterization of smaller device sizes and surface interfaces. In-line XPS tooling was introduced in 2004 as a metrology solution to some of the challenges in the 65 nm node and beyond [1,2]. At that time, ellipsometry had reached accuracy limitations for the small film thickness variations of gate stack materials that could, however, be characterized with the highly surface and material sensitive, non-destructive analytical properties of XPS. The technique increased in relevancy as industry specifications drove the control of film thickness tolerances to sub-nm levels and new materials continued to be incorporated into different layers [3]. While XPS measurement areas have generally been relegated to unpatterned wafers or blanket film metrology pads on integrated wafers, the technique and modeling capabilities have continually evolved to incorporate some direct measurement on fully integrated structures and device areas [4]. In 2015, working XPS models on structure have been published including a pitch-dependent monitor for Cu chemical mechanical polish (CMP) process control [5]. Later developments cover a wide ranger of applications including direct measurement of dopant material composition of source drain (S/D) pFET epi structures [6] and for area-selective deposition processes on patterned structure [7]. This trend is expected to become more relevant as scaling pushes towards smaller structural dimensions, resulting in greater potential deviations between metrology on blanket targets and 3D integrated structure.

Additional challenges for XPS measurement integration include characterization of Nanosheet gate-all around (GAA) transistor architectures. Because XPS spectra and intensities include and are weighted respectively by all the materials present in the near surface regions of the measurement area, XPS modeling is only as accurate as the ability to fully characterize the respective spectra obtained. However, the precision of measurement is substantially improved if the proper material quantifications and structural dimensions are established and defined appropriately.

In this paper, we first discuss XPS model developments necessary to enable blanket film thickness measurement on GAA film stacks. We then demonstrate how XPS may be employed as a direct metrology technique on fully integrated targets

Metrology, Inspection, and Process Control XL, edited by Nivea G. Schuch,
Hugo Cramer, Proc. of SPIE Vol. 13981, 139810A · 2026 Published by
SPIE · 0277-786X · doi: 10.1117/12.3091932

and device areas. Several applications are highlighted including S/D epi composition, parasitic epi growth in S/D region, and quantification of residues following removal via CMP processes. In addition, we highlight a hybrid metrology application where the XRF emission and spectra generated during XPS measurement is utilized to quantify embedded SiGe layers beyond limited depth of XPS penetration.

2. EXPERIMENTAL DETAILS

2.1 Experimental setup

XPS is a technique that utilizes the photoelectron spectra generated from an X-ray source to determine the chemical and dimensional properties from the surface region of the sample. The fundamental interactions are illustrated in Fig. 1a where an X-ray excites a core level electron in the sample, simultaneously ejecting a photoelectron and leaving behind a core level hole. An electron from a higher shell may then relax into this hole and subsequently release the excess energy as X-ray fluorescence (XRF) or through the ejection another higher core electron, defined as an Auger electron emission. A general setup for XPS measurement (Fig. 2b) consists of an X-ray source which bombards a sample with monochromatic X-rays. A finite solid angle of the ejected photoelectrons corresponding with the aperture size are passed through and filtered by kinetic energy through the electron optics column and hemispherical energy analyzer before terminating at the electron detector. These photoelectron detection events may then be converted into spectra categorized by kinetic energy and signal intensity, or electron count rate, of the detected photoelectrons. Figure 1c shows an example survey scan for a TiO_2 sample generated with all photoelectron excitation and Auger ejection peaks labelled.

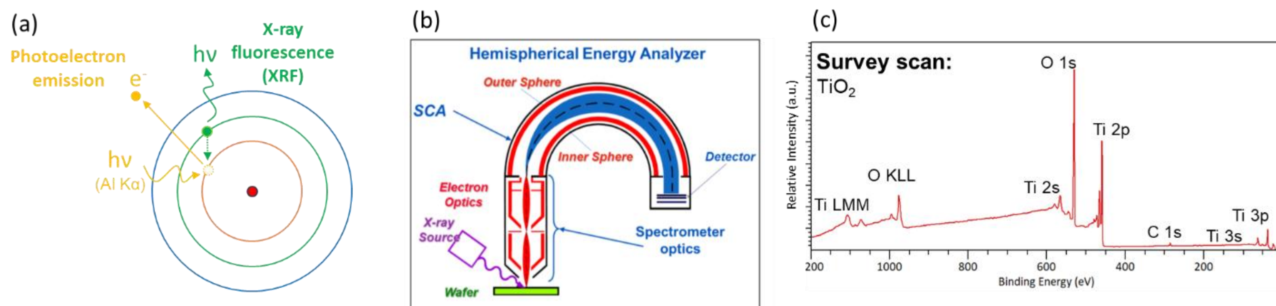

Figure 1. (a) Simplified representation illustrating the photoelectron emission and X-ray fluorescence events following the X-ray excitation of an z. (b) Schematic of an XPS measurement setup. (c) XPS spectra of a TiO_2 sample with photoelectron excitation and Auger peaks labeled.

While laboratory based XPS instrumentation and measurements are often designed to widely characterize a new material or process with a higher resolution and wider spectral output, in-line XPS measurements are engineered tightly around target materials and processes that have been otherwise characterized beforehand. Once an in-line XPS measurement routine can reliably quantify variation from a process baseline, the primary recipe design goal is to minimize measurement time much as possible to improve fab productivity. Recipe side optimizations include the minimization of spectral acquisition ranges, measurement scan time, and the number and location of measurements per wafer. Throughput optimizations on the tool side include standardization of instrumental configuration to a singular X-ray source, fixed photoemission angle to the detector, and a fixed high analyzer pass energy to maximize photoelectron flux. As XPS measurements require high-quality vacuum conditions $< 5\times10^{-7}$ Torr in an analysis chamber, throughput delays are minimized by staging wafers in queue in a pre-chamber load lock. This allows for simultaneous pump down of incoming wafers to appropriate vacuum levels while the active wafer is being measured in the analysis chamber.

Measurements in this study were taken on a Nova VeraFlex IV XPS tool platform, capable of fully automated in-line processing of 300 mm wafers. This tool produces AlKα X-rays in a 50 µm diameter spot, allowing for measurement on fully integrated metrology targets equal to or greater than these dimensions. The electron detector in the setup utilizes a spherical capacitor analyzer (SCA) for XPS photoelectron detection. A secondary silicon drift detector (SDD) is installed on a side port on the instrumental chamber and allows for the capture and analysis XRF as well.

2.2 Photoelectron attenuation modeling

In order to provide meaningful quantification of collected XPS spectra, measurements rely on understanding and modeling the photoelectron yield and attenuation as the electrons move and scatter during their travel through measured material.

While a full review of these mechanisms is beyond the scope of this manuscript, many other studies provide a more comprehensive overview of these interactions, including fundamentals of spectral interpretation and peak fitting [8-13]. Figure 2a illustrates the potential travel pathway of photoelectrons generated at several depths of a sample. As photoelectrons travel further through material layers, there is a larger probability that the photoelectron will undergo single or multiple scattering events, both inelastic and elastic. The expected reduction in photoelectron yield as a function of travel length and scattering can be characterized the effective attenuation length (EAL) [14]. This is dependent on the kinetic energy of the photoelectron as well as the material traversed in the path of the photoelectron. Photoelectrons generated near the surface of the film are less likely to scatter than photoelectrons generated in the bulk levels and therefore provide the highest intensity yield.

Figure 2b shows a model depiction of the intensities generated from an SiO/Si film stack and Fig. 2c shows the modeled Si and SiO intensities as a function of film thickness. In this scenario, the intensity of Si scales according to the equations below

$$I_{Si} \propto e^{\left(-\frac{d_{SiO}}{EAL_{SiO}}\right)} \quad (1)$$

$$I_{SiO} \propto 1 - e^{\left(-\frac{d_{SiO}}{EAL_{SiO}}\right)} \quad (2)$$

where I_{Si} is the intensity of Si, I_{SiO} is the intensity of SiO, d_{SiO} is the thickness of SiO, and EAL_{SiO} is the EAL of Si photoelectrons travelling through the SiO layer. The thickness of the SiO layer can be extracted from the measurement by scaling the Si and SiO intensities accordingly. These exponential sensitivity properties of XPS enable the precise detection of small changes in ultrathin films < 2 nm while the bulk scattering generally results in the effective loss of measurement sensitivity beyond > 10 nm of material when utilizing an Al Kα X-ray source.

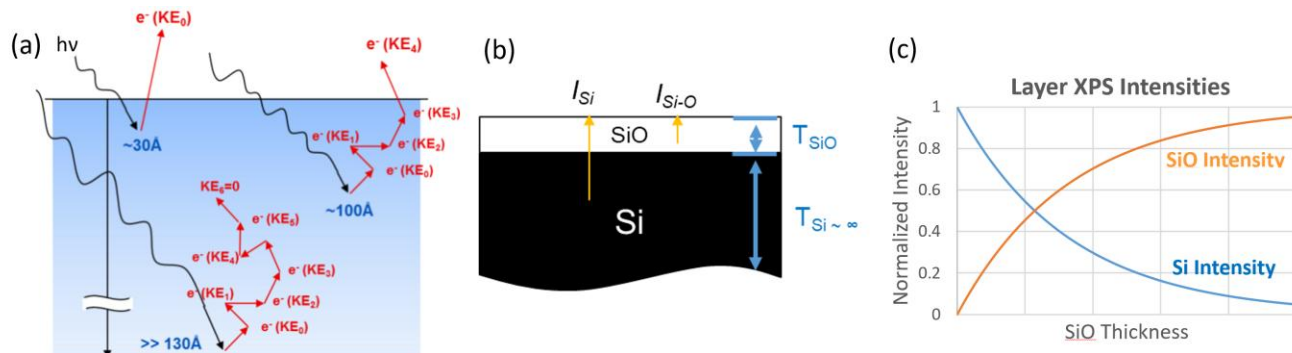

Figure 2. (a) Illustration for photoelectron excitation and electron scattering from the surface and bulk depths of sample. (b) Model depiction of a SiO overlayer on top of a semi-infinite Si substrate along with corresponding (c) XPS SiO and Si intensities as a function of SiO overlayer thickness.

3. RESULTS AND DISCUSSION

3.1 Nanosheet blanket models

Layer-by-layer stack thickness measurements can generally be quantified with a high degree of precision using XPS so long as each layer of interest has a unique, identifiable peak in the XPS spectra. However, modelling the Nanosheet GAA stack consists of alternating Si and SiGe layers, both of which contribute separately to the intensity of the XPS Si peaks. This introduces error into the XPS measurement to any layers above the top Si sheet unless the contributions to the net Si intensity are properly attributed to their corresponding layers.

An example of this is seen when comparing similar thicknesses of an interlayer (IL) dielectric grown on a directly on Si (Fig. 3a) compared to IL grown on a SiGe supported Si top sheet (Fig. 3b). While the XPS SiO intensity is similar between the two stacks (Fig. 3c), the Si intensity is measurably lower for the measurement on the Nanosheet stack. The traditional IL model has been built with the assumption that all the intensity from Si (I_{Si}) comes from the Si substrate. However, the IL grown on a GAA Nanosheet stack has a lesser Si contribution since the Si content is more dilute in the SiGe layer compared to Si of a comparable depth and thickness.

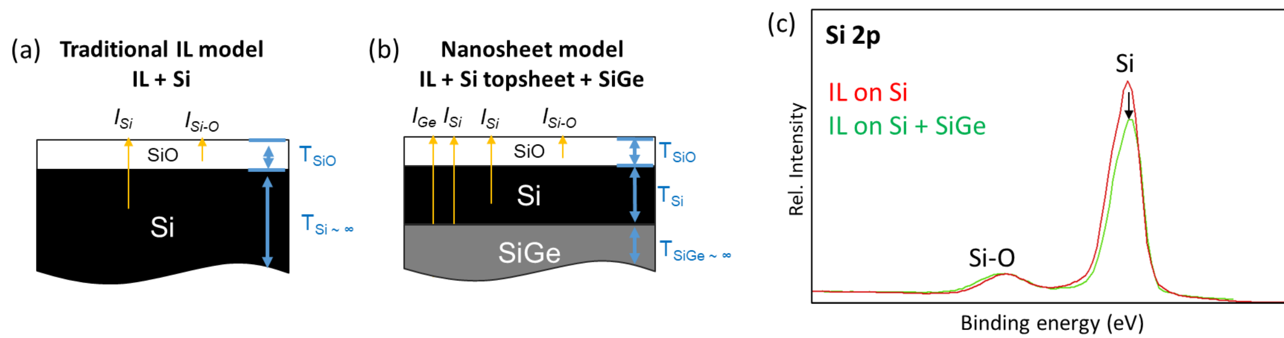

Figure 3. Schematics for the blanket layer assumptions for the (a) traditional IL model on Si and (b) IL model with Si top sheet and SiGe underlayer. (c) XPS Si 2p spectra for IL grown on Si (red) and IL grown on Si/SiGe (green).

Nanosheet correction and top sheet extraction

Figure 4a shows an illustration of the Nanosheet stack consisting of alternating Si and SiGe layers along with an overlayed chart of XPS signal intensity as function of distance to surface. This plot indicates that while most of the underlayers provide insignificant intensity contributions, the topmost SiGe layer still contributes substantially and must be considered in the model. Spectral contributions are shown for Ge (Fig. 4b) and Si (Fig. 4c), which includes both the Si contributions from the Si top sheet as well as the topmost SiGe layer. These Si contributions must be separated and applied to the appropriate layers in order to produce an effective model. After using the SiGe Ge percentage as a model input, the following intensity correction for the Si top sheet layer can be applied as follows

$$I_{Si,correct} = I_{Si,measured} - CF \cdot I_{Ge,measured} \tag{3}$$

where $I_{Si,correct}$ is the corrected Si top sheet intensity, $I_{Si,measured}$ is the total measured Si peak intensity, $I_{Ge,measured}$ is the measured Ge intensity, and CF is the conversion factor used to relate the Ge and Si intensities from the SiGe layer.

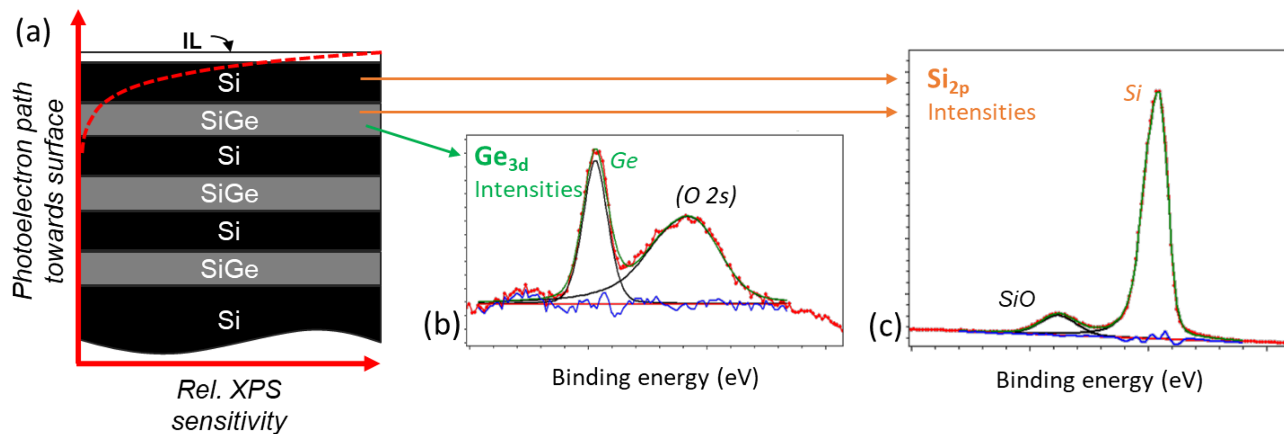

Figure 4. XPS Ge 3d and Si 2p peak fitting and intensity extraction for (a) Process A and (b) Process B. (c) Si top sheet thickness output for the Nanosheet model for Process A and Process B.

Beyond the IL thickness correction, the Si intensity correction allows for the measurement of the Si top sheet thickness. The results of this model for two separate process treatments on the Nanosheet stack are shown with corresponding spectra, labelled as Process A (Fig. 5a) and Process B (Fig. 5b). Process B shows significantly higher Ge and Si intensities and substantially lower SiO intensities compared to Process A. Figure 5c shows that when the Nanosheet model is applied to spectra from these processes, Process A clearly exhibits a larger Si thickness than process B. In addition, both the processes and the model provide a stable cross-wafer baseline for Si thickness.

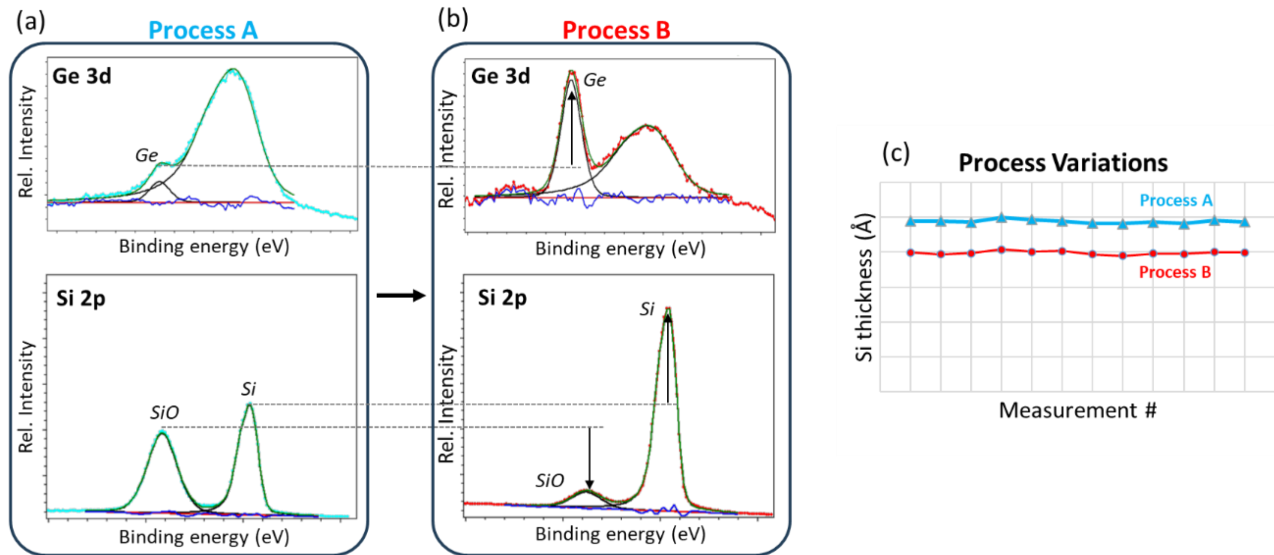

Figure 5. XPS Ge 3d and Si 2p peak fitting and intensity extraction for (a) Process A and (b) Process B. (c) Si top sheet thickness output for the Nanosheet model for Process A and Process B.

Nanosheet correction for high-k gate stack layer

In addition, this correction can be extended to any subsequent layers added to the Nanosheet stack. Here we discuss the improvements when applying the Nanosheet after the addition of the high-k dielectric layer. Figure 6a illustrates a model depiction of the Nanosheet film stack following high-k dielectric deposition and corresponding spectra for a smaller Si top sheet thickness (Fig. 6b) and a larger Si top sheet thickness (Fig. 6c). In this case, new peak fitting must be applied to deconvolute the Ge intensities from the additional high-k spectral contributions. While the Ge intensities decrease at larger Si top sheet thicknesses, small Ge intensities can still be extracted with proper peak fitting as seen in the spectra. The Nanosheet correction may be applied so long as the Ge intensity can be extracted consistently and reliably.

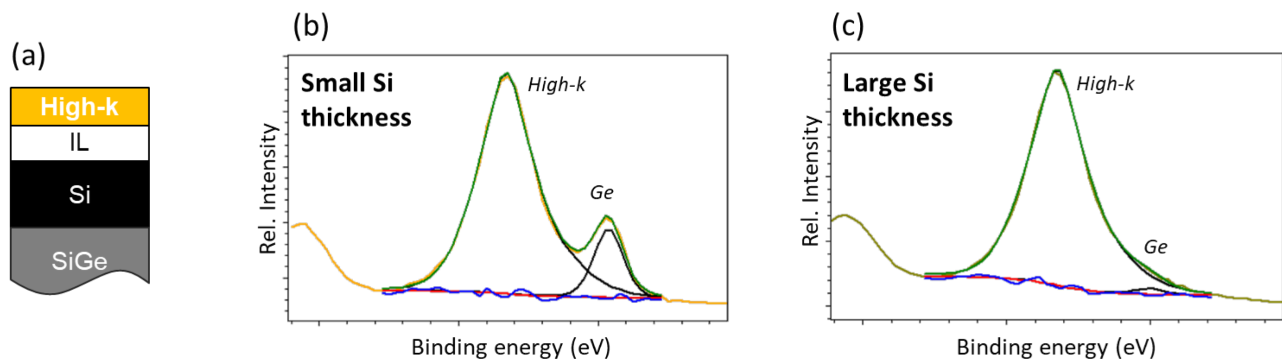

Figure 6. (a) Schematic of XPS blanket model for high-K dielectric on Si/SiGe as a proxy for Nanosheet GAA. XPS Spectra capturing the deconvolution of the high-K contribution from Ge for (b) a smaller Si top sheet thickness and (c) a larger Si top sheet thickness.

Figure 7a shows the effect on XPS measurement output for high-k thickness when modeled on a Si substrate compared to the Nanosheet stack. Nominal Si thicknesses were calibrated using X-ray diffraction measurements for and compared to the output from the XPS models. In the case of the Si substrate model, the XPS high-k thickness is greatly distorted at the lower end of nominal Si thickness measurements. However, the Nanosheet model correction flattens out the high-k thickness over all ranges of nominal Si thicknesses. In addition, Fig. 7b shows that the XPS Si thickness scales linearly with the nominal XRD calibrated thickness. The linearity of the model breaks only at much larger Si top sheet thicknesses where the reference Ge intensities become vanishingly small. The Nanosheet model therefore provides a robust method of monitoring Si top sheet thickness, particularly with smaller film thickness dimensions.

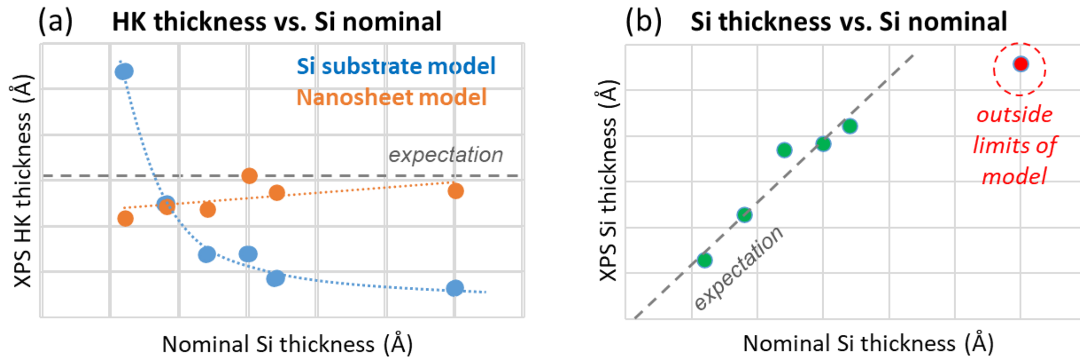

Figure 7. (a) Calculated high-k thickness from Si and Nanosheet models and (b) calculated Si thickness from Nanosheet model measured from wafers with variable nominal Si top sheet thicknesses.

3.2 XPS measurements on structure

XPS characterization of integrated structure introduces additional modeling challenges compared to blanket film stacks as the measurement dimensionality changes from 1D to 3D. These measurements must account for any spectral contributions from material differences in the lateral directions in addition to the in-plane composition and thickness variations with respect to the wafer surface. In these scenarios, it is advantageous to apply hard modelling constraints to structural parameters and limit the solution variable space while leveraging the strengths of XPS measurements. This includes limiting analysis to the high sensitivity near surface structural elements, applying robust peak fitting to differentiate compositional to isolate regions of interest from other spectral contributions, and constraining known 2D and 3D parameters based on knowledge of the process and structures.

S/D characterization on fully integrated targets

XPS has previously been utilized to characterize SiGe composition for both the Nanosheet GAA blanket stacks as well as the dopant concentrations for S/D regions on structure [6,15,16]. In the following example, the extraction of the Ge % composition directly from the S/D regions of the structure is highlighted. The schematic in Fig. 8a shows a structure with after S/D epitaxy. The measured intensity from the S/D epi is expected to be smaller since the epi accounts for a smaller fraction of the exposed measurement area. The epi intensity is further diminished due to the taller dimensions of the sidewall structures which narrows the acceptable photoelectron ejection trajectory to the detector. This is observed from the spectra in Fig. 8b where the Si intensities from the S/D epi are substantially smaller than the other structural Si contributions. Fig. 8c shows that that after accounting for scale, the signal to noise of the Ge intensities are lower compared to the background level. Nonetheless, proper peak fitting enables the separation of the Si and Ge intensities specifically from the S/D region epi so that SiGe Ge % composition can be calculated. Figure 8c shows the results of this model applied to measurements on integrated targets with variable structural pitches. The cross-wafer averages show small differences but measurable decreases in Ge % as a function of changing pitch in order of Macro A, Macro B, and Macro C. A calibrated model for measurements on structure is highly desirable as shown here, where structural design variations directly affect the material properties following the same process step.

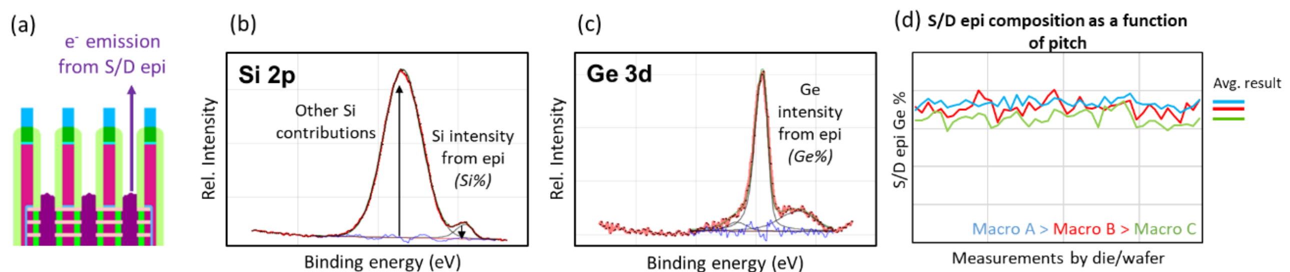

Figure 8. (a) Model of a structure with exposed S/D epi along with the photoemission path for epi measurement characterization. XPS spectra for (b) Si 2p and (c) Ge 3d showing intensity contributions from S/D epi and other structure. (d) Plot of S/D epi Ge % as a function of different structural pitches.

Parasitic nFET-epi growth on pFET S/D epi

In the next example, we discuss a method using XPS to monitor parasitic epi growth on pFET S/D epi structures. Parasitic epi growth is a consequence of epi deposition processes where epi nucleates in unintended regions and negatively impacts device performance [17]. While many variations of parasitic growth exist, here we discuss using XPS to monitor a specific form of parasitic epi growth in the form of nFET epi nodules on active pFET S/D regions as depicted in Fig. 9a. In this case, some inhomogeneity in the process flow allows for nFET epi nodules to grow directly on the active pFET S/D region following nFET epi deposition. Because the nFET epi contains P while the pFET epi is free of any P content, XPS P 2p spectra can be used to detect the presence of nFET nodules on the surface of pFET S/D regions. This is shown in Fig. 9b where a structure with parasitic nFET nodules shows an elevated P 2p peak while the same region for a clean, functional pFET epi target is flat in that same region. By quantifying these P 2p peak intensities (Fig. 9c a clear elevated threshold for P intensity counts is observed and established compared to the lower baseline for the functional pFET epi region. This enables faster cycles of feedback directly after the nFET deposition so that processes can be optimized to minimize parasitic epi growth well before comprehensive defect inspection and device yield tests.

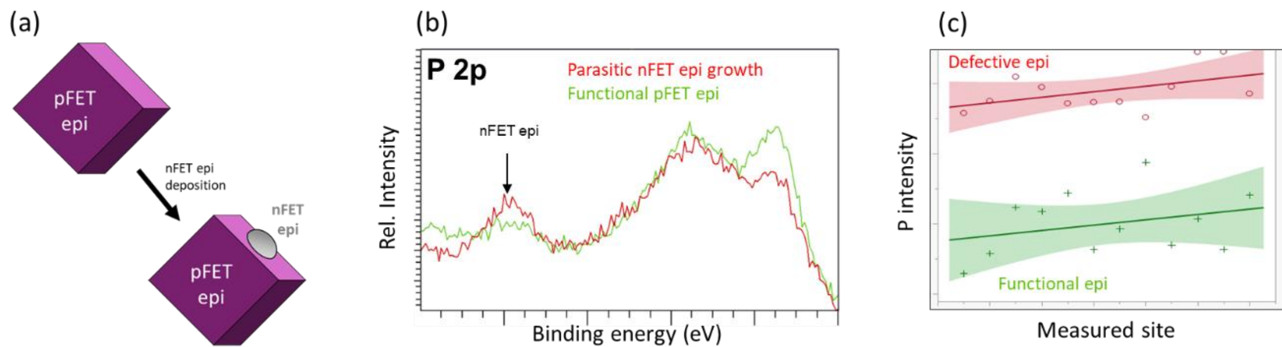

Figure 9. (a) Schematic of a clean pFET epi structure and pFET epi structure with parasitic nFET epi growth. (b) XPS P 2p spectra for a clean pFET structure (green) and pFET epi structure with parasitic nFET epi growth (red). (c) Quantification of XPS P 2p spectra for a functional pFET epi (green) and defective pFET epi (red).

Residue CMP removal monitor on integrated targets and device area

One key advantage of XPS measurement on structure is the enhanced sensitivity to the surface of measured target area. This makes the technique particularly powerful for determining whether material present is exposed to the surface or enclosed by another material with a separate composition. The following application highlights XPS as a way to monitor surface residues structure post CMP processes. This methodology can be applied to both integrated target structure and actual device areas.

Figure 10a shows a schematic of a device structure prior to CMP processing intended to remove the surface residue layer to reveal the structure underneath. In the schematic, the surface residues are labelled as the highest sensitivity to XPS while the structure below has a lower sensitivity. Any structure below these regions provides negligible intensity contributions to the spectra due to the larger depth from the surface of the measured region. Figure 10b shows the XPS spectra region of interest for measurements on structure for a region with residues present and with the residues fully removed. The spectra for a structure with residues fully removed consists primarily of intensity region and peak area labelled as B, corresponding with intensity coming from the primary structure to be revealed. In contrast, the spectra from a structure with residues shows an elevated level of intensity from the spectral region labelled as A, corresponding with the larger presence of residue materials. This interpretation is validated by TEM images taken along with the XPS measurements for a device with underpolished structure (Fig. 10c) and a fully polished device with structure clear of residues (Fig. 10d).

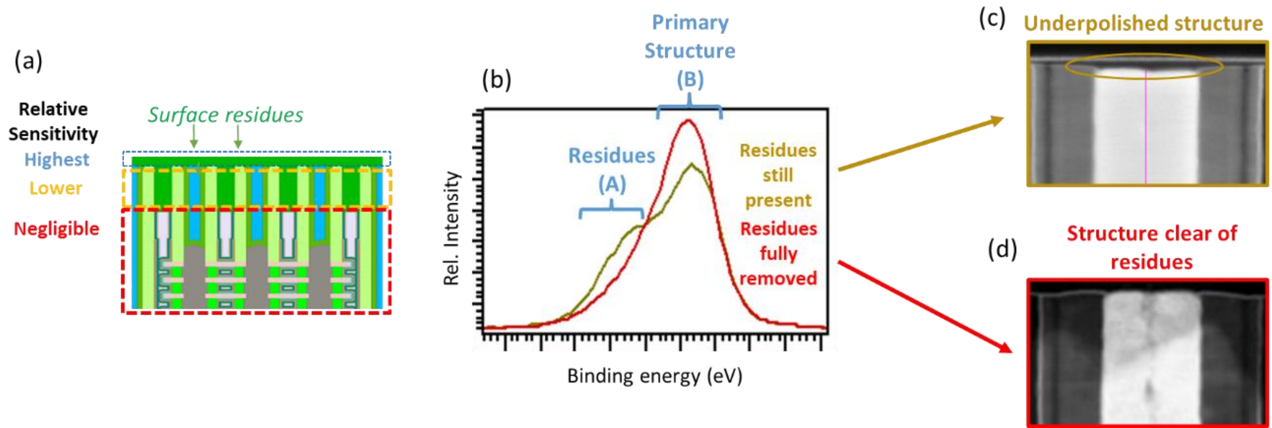

Figure 10. (a) Schematic of fully integrated structure utilizing XPS to validate full surface residue. (b) Comparison of XPS spectra with residues and with residues removed and representative TEM images of structure with (c) residues present and (d) residues removed.

The progress towards clearing the surface of residues and revealing the underlying structure via CMP processes can then be monitored as intensity ratio A/B, representing relative intensity contributions from residues to structure. Figure 11a shows a box plot of ratio A/B measurements across fully integrated targets on a wafer following multiple rounds of the CMP process. After the first round, both the overall value and the relative measurement spread of these ratios are elevated across the wafer. These results are in agreement with larger amounts of residue still present on the wafer and inhomogeneous residue removal. However, both the ratio and the spread drop precipitously after the second and third rounds with some of the dies reaching a plateau at a low ratio value. By the fourth round, all the dies have settled homogeneously on this low intensity ratio plateau, indicating that the integrated target structures on wafer are free of residues.

Figure 11b shows another example of cross wafer residue intensity ratios as a function of radial position. These measurements were taken directly on device areas following CMP processes, one of which resulted in a clean wafer and another wafer with edge residues. The central areas of both wafer exhibit minimal residue ratio values, indicating that the CMP processes are both effective in clearing the center of the wafer. However, the wafer with edge residues shows a continual growth in residue intensity when moving radially outward from the center, indicating that the CMP process for this wafer is less effective at the edges.

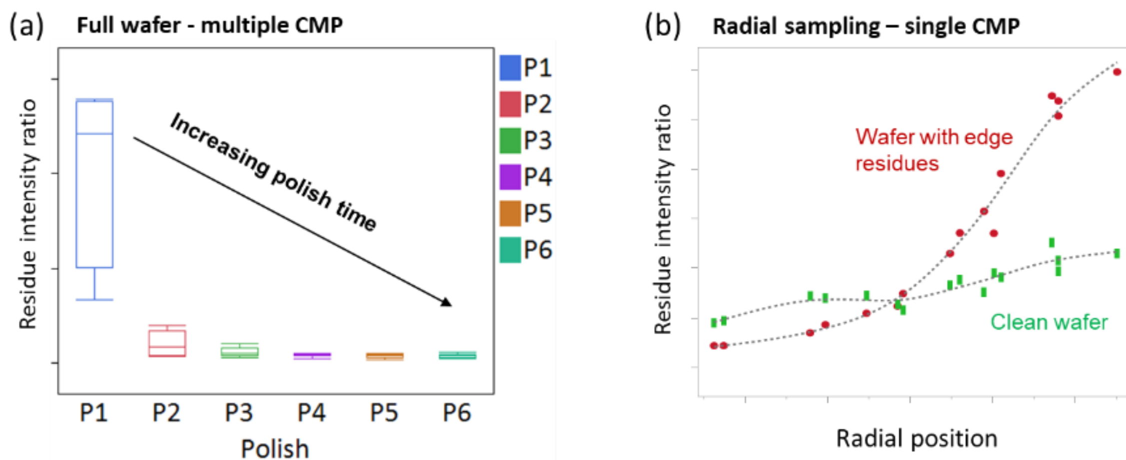

Figure 11. XPS residue to structure (A/B) intensity ratios following (a) multiple CMP cycles across wafer and after (b) process optimization for center to edge variation.

The dimensionless nature of these results, characterized as an accelerated dip in the residue to structure ratio followed by a plateau region, gives this surface characterization the flexibility to be applied broadly over a range of structural designs.

As long as the intensity ratio plateau threshold is properly established for the measured regions of a clean wafer, this model can be extended to provide meaningful, quantifiable results on actual device areas in addition to fully integrated targets, providing the closest point of reference for actual device performance.

XRF for SiGe indent and channel release

With the addition of an XRF detector to an in-line XPS setup, XRF spectra can be acquired simultaneously with XPS spectra collection without any additional spectral acquisition time. In addition, XRF emissions are attenuated at a much larger length scale compared to the electron scattering lengths of photoelectrons and therefore are not subject to the same sampling depth limitations. This enables a much simpler quantification for XRF results as the total intensity from an XRF excitation scales linearly with the amount of the material of interest captured in the measured structure.

XRF has long been evaluated as an option to characterize changes in the embedded SiGe layers within GAA stacks [18-20]. Here we discuss a method to characterize SiGe channel indent depth initially conducted by Schmidt et al. using a hybrid metrology approach with XRF and optical critical dimension (OCD) metrology [21,22]. In this study, the Ge Lα obtained from the XRF was used to quantify the volumetric change in SiGe content before and after SiGe indent. This data was then used along with an optical critical dimension (OCD) measurement in order to constrain the structural parameter space output by the subsequent model. By taking this hybrid metrology approach, the XRF-enhanced OCD model converts the volumetric changes from the Ge Lα counts into a specific indent depth for the SiGe layers separating the Nanosheets. Beyond this application, the Ge Lα XRF counts can be used to quantify any residual SiGe content following post channel release processes intended for full SiGe layer removal. Figure 12a shows the XRF spectra progression in order of decreasing Ge Lα for pre indent (Fig. 12b), post indent (Fig. 12c), and post channel release processes (Fig. 12d). As the Ge Lα excitations are insensitive to any surrounding structure, XRF can be used to monitor changes in the embedded SiGe layers through multiple steps throughout the full process flow.

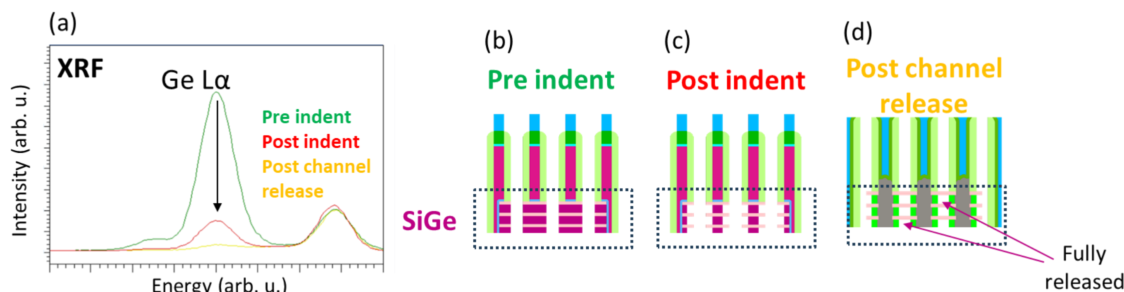

Figure 12. (a) XRF Ge Lα spectra collected over the course of several SiGe removal processes along with process schematics for (b) pre indent, (c) post indent, and (d) post channel release.

4. SUMMARY AND CONCLUSIONS

In this work, we have shown a novel method to improve XPS modeling to compensate for the finite thickness alternating Si and SiGe layers in Nanosheet GAA film stacks. Furthermore, it was demonstrated that XPS measurement capabilities have progressed beyond characterization limited to blanket films to the point of meaningful measurement on fully-integrated target and device areas. This includes the selective characterization of S/D epitaxy to determine pitch-dependent Ge %, parasitic epitaxial growth on the S/D regions, and the monitoring of material surface residues post CMP processes, for example. With parallel in-line XRF capabilities, it was also highlighted how the complementary XRF intensities can be utilized to measure volumetric in embedded materials beyond the limits of XPS penetration depth, and that these inputs can be integrated in a hybrid metrology setup with OCD to determine actual structural parameters. Measurement directly on integrated targets and active device areas are superior since it removes the need to account for differences in process outcomes on structure compared to proxy, blanket film stacks. As the application of XPS measurements expands to measurement on fully integrated structures, further development of modeling capabilities is needed to meet the growing complexity.

ACKNOWLEDGEMENTS

The authors would like to thank Susan Emans (IBM) for fruitful discussions as well as IBM and Nova management for support of this work.

REFERENCES

[1] https://www.eetimes.com/revera-starts-life-with-a-tool-for-gate-metrology-2/

[2] https://www.metrologyworld.com/doc/revera-announces-the-veraflex-materials-metro-0001/

[3] C.R. Brundle, G. Conti, and P. Mack, “XPS and angle resolved XPS, in the semiconductor industry: Characterization and metrology control of ultra-thin films,” J Electron Spectros Relat Phenomena 178–179(C), 433–448 (2010).

[4] A. Vaid, G. Iddawela, S. Mahendrakar, M. Lenahan, M. Hossain, P. Timoney, A.F. Bello, C. Bozdog, H. Pois, W.T. Lee, M. Klare, M. Kwan, B.C. Kang, P. Isbester, M. Sendelbach, N. Yellai, P. Dasari, and T. Larson, “Hybrid enabled thin film metrology using XPS and optical,” Proc. SPIE 9778, Metrology, Inspection, and Process Control for Microlithography XXX, 97780M (2016).

[5] B. L’Herron, R. Chao, K. Kim, W.T. Lee, K. Motoyama, B. Deprospo, T. Standaert, J. Gaudiello, and C. Goldberg, “Hybridization of XRF/XPS and scatterometry for Cu CMP process control,” Proc. SPIE 9424, Metrology, Inspection, and Process Control for Microlithography XXIX, 94241M (2015).

[6] J. Lee, G. Subramanian, M. Medikonda, H. Lazkani, J. Holt, C. Gaire, P. Isbester, and M. Klare, “Full structure transistor process monitoring of boron and germanium in PFET EPI using in-line XPS,” Proc. SPIE 10959, Metrology, Inspection, and Process Control for Microlithography XXXIII, 109590N (2019).

[7] M. Medikonda, L. Wangoh, C.J. Lee, M. Klareb, D. Kislitsynb, H. Pois, P. Isbester, A. Cepler, W.T. Lee, and D. Schmidt, “In-line XPS metrology for area-selective deposition processes on patterned structures,” Proc. SPIE 13891, Metrology, Inspection, and Process Control XL, 13981-35 (2024).

[8] A.G. Shard, “Practical guides for x-ray photoelectron spectroscopy: Quantitative XPS,” Journal of Vacuum Science & Technology A: Vacuum, Surfaces, and Films 38(4), 041201 (2020).

[9] M.H. Engelhard, D.R. Baer, A. Herrera-Gomez, and P.M.A. Sherwood, “Introductory guide to backgrounds in XPS spectra and their impact on determining peak intensities,” Journal of Vacuum Science & Technology A: Vacuum, Surfaces, and Films 38(6), 063203 (2020).

[10] G.H. Major, N. Fairley, P.M.A. Sherwood, M.R. Linford, J. Terry, V. Fernandez, and K. Artyushkova, “Practical guide for curve fitting in x-ray photoelectron spectroscopy,” Journal of Vacuum Science & Technology A: Vacuum, Surfaces, and Films 38(6), 061203 (2020).

[11] C.D. Wagner, L.E. Davis, M. Zeller, J.A. Taylor, R.H. Raymond, and L.H. Gale, “Empirical atomic sensitivity factors for quantitative analysis by electron spectroscopy for chemical analysis,” Surface and Interface Analysis 3(5), 211–225 (1981).

[12] S. Doniach and M. Sunjic, “Many-electron singularity in X-ray photoemission and X-ray line spectra from metals,” Journal of Physics C: Solid State Physics 3(2), 285 (1970).

[13] S. Tougaard, “Practical guide to the use of backgrounds in quantitative XPS,” Journal of Vacuum Science & Technology A: Vacuum, Surfaces, and Films 39(1) (2021).

[14] C.J. Powell and A. Jablonski, “Surface sensitivity of X-ray photoelectron spectroscopy,” Nucl Instrum Methods Phys Res A 601(1–2), 54–65 (2009).

[15] B. L’herron, N. Loubet, Q. Liu, S. Farhat, J. Fullam, J. Gaudiello, S. Rangarajan, B. Sun, W.T. Lee, M. Klare, H. Pois, M. Kwan, Y. Wang, T. Larson, R. Wacquez, and S. Maitrejean, “Silicon-Germanium (SiGe) composition and thickness determination via simultaneous smallspot XPS and XRF measurements,” 25th Annual SEMI Advanced Semiconductor Manufacturing Conference (ASMC), 26–30 (2014).

[16] G.R. Muthinti, N. Loubet, R. Chao, A.A. de la Peña, J. Li, M.A. Guillorn, T. Yamashita, S. Kanakasabapathy, J. Gaudiello, A.J. Cepler, M. Sendelbach, S. Emans, S. Wolfling, A. Ger, D. Kandel, R. Koret, W.T. Lee, P. Gin, K. Matney, et al., “Materials characterization for process integration of multi-channel gate all around (GAA) devices,” Proc. SPIE 10145, Metrology, Inspection, and Process Control for Microlithography XXXI, 101451U (2017).

[17] D. Kong, R. Chao, M. Breton, C. Liu, G.R. Muthinti, S. Seo, N.J. Loubet, P. Montanini, J. Gaudiello, V. Basker, A. Cepler, S. Ng-Emans, M. Sendelbach, I. Kaplan, G. Barak, D. Schmidt, and J. Frougier, “In-line characterization of non-selective SiGe nodule defects with scatterometry enabled by machine learning,” ," Proc. SPIE 10585, Metrology, Inspection, and Process Control for Microlithography XXXII, 1058510 (2018).

[18] R. Muthinti, N. Loubet, R. Chao, J. Ott, M. Guillorn, N. Felix, J. Gaudiello, P. Lund, A. Cepler, M. Sendelbach, O. Cohen, S. Wolfling, C. Bozdog, and M. Klare, "Advanced in-line optical metrology of sub-10nm structures for gate all around devices (GAA)," Proc. SPIE 9778, Metrology, Inspection, and Process Control for Microlithography XXX, 977810 (2016).

[19] D. Kong, D. Schmidt, M. Breton, A.A. de la Peña, J. Frougier, A. Greene, J. Zhang, V. Basker, N. Loubet, I. Ahsan, A. Cepler, M. Klare, M. Cheng, R. Koret, and I. Turovets, "Development of SiGe Indentation Process Control to Enable Stacked Nanosheet FET Technology," 2020 31st Annual SEMI Advanced Semiconductor Manufacturing Conference (ASMC), 1–5 (2020).

[20] J. Bogdanowicz, Y. Oniki, K. Kenis, Y. Muraki, T. Nuytten, S. Sergeant, A. Franquet, V. Spampinato, T. Conard, I. Hoflijk, J. Meersschaut, N. Claessens, A. Moussa, D. van den Heuvel, J. Hung, R. Koret, A.-L. Charley, and P. Leray, "Spectroscopy: a new route towards critical-dimension metrology of the cavity etch of nanosheet transistors," Metrology, Inspection, and Process Control for Semiconductor Manufacturing XXXV, 116111Q (2021).

[21] D. Schmidt, C. Durfee, S. Pancharatnam, M. Medikonda, A. Greene, J. Frougier, A. Cepler, G. Belkin, D. Shafir, R. Koret, R. Shtainman, I. Turovets, and S. Wolfling, "OCD enhanced: implementation and validation of spectral interferometry for nanosheet inner spacer indentation," Proc. SPIE 11611, Metrology, Inspection, and Process Control for Semiconductor Manufacturing XXXV, 116111U (2021).

[22] D. Schmidt, A. Cepler, C. Durfee, S. Pancharatnam, J. Frougier, M. Breton, A. Greene, M. Klare, R. Koret, and I. Turovets, "Development of SiGe Indentation Process Control for Gate-All-Around FET Technology Enablement," IEEE Transactions on Semiconductor Manufacturing 35(3), 412–417 (2022).